Physics of Fluids

RESEARCH ARTICLE | FEBRUARY 21 2025

Wind load interference mechanisms for inclined angle and gap spacing of photovoltaic panels

Tingting Liu (刘婷婷) ; Hanning Mi (米翰宁); Yifeng Ai (艾轶峰); Hongfu Zhang (张洪福) ✉ ;
Daocheng Zhou (周道成); Lei Zhou (周蕾)

Physics of Fluids 37, 023623 (2025)
https://doi.org/10.1063/5.0249576

AIP Publishing

Physics of Fluids ARTICLE pubs.aip.org/aip/pof

Wind load interference mechanisms for inclined angle and gap spacing of photovoltaic panels

Cite as: Phys. Fluids **37**, 023623 (2025); doi: 10.1063/5.0249576
Submitted: 19 November 2024 · Accepted: 3 January 2025 ·
Published Online: 21 February 2025

Tingting Liu (刘婷婷),[1] Hanning Mi (米翰宁),[2] Yifeng Ai (艾轶峰),[3] Hongfu Zhang (张洪福),[4,a)]
Daocheng Zhou (周道成),[1] and Lei Zhou (周蕾)[5]

AFFILIATIONS

[1]School of Civil Engineering and Transportation, Northeast Forestry University, Harbin, Heilongjiang Province, China
[2]China Electric Power Research Institute, Beijing, China
[3]Department of Architecture and Civil Engineering, City University of Hong Kong, Hong Kong, China
[4]Department of Mechanical Engineering, The Hong Kong Polytechnic University, Hong Kong, China
[5]School of Civil Engineering, Central South University, Changsha, Hunan Province, China

[a)]Author to whom correspondence should be addressed: zhanghongfu@nefu.edu.cn

ABSTRACT

This study aims to explore wind load interference effects on tandem photovoltaic (PV) panels, focusing on inclined angles (α) and gaps (X/L). Conventional models often struggle to capture nonlinear airflow dynamics that drive these interference effects. To address this limitation, the research introduces a novel approach to analyze the complex spatiotemporal evolution of interference phenomena in PV panels. A quantitative analysis was conducted using the high-order Koopman Mode Decomposition (HOKMD) method. This method integrates high-order nonlinear components, enabling precise identification of dynamic modes and coherent structures. This study evaluates the synchronous vorticity and pressure fields, fluid forces, and power spectra of PV panels under varying α and X/L. The results demonstrate that for $\alpha > 25°$ and $X/L < 2.0$, interference effects are highly pronounced, while for $X/L > 2.0$, significant shielding effects are observed on the downstream panel. It revealed two dominant dynamic modes, providing new insights into airflow patterns and vortex interactions that traditional linear models fail to capture. The application of HOKMD accurately captures the nonlinear characteristics of the flow around PV panels. The findings advance the understanding of airflow interactions in PV panels and provide valuable insights for optimizing PV design to improve structural stability and durability.

NOMENCLATURE

A	Best-fitting linear mapping system.
a_i	Mode amplitude.
B	Low-dimensional subspace.
Cd	Drag force coefficient.
Cl	Lift force coefficient.
Cp	Pressure coefficient on PV panels.
E_i	Mode energy.
f	Vortex shedding frequency.
F_d	Drag force of the panel per unit length.
F_L	Lift force of the panel per unit length.
G	Ground clearance of PV panels.
L	Length of the PV panel.
L'	Projected width of the panel perpendicular to the wind.
M	Projection operator.
p	Fluid pressure.
p_0	Static pressure.
R	Residual matrix.
Re	Reynolds number.
St	Strouhal number.
u	Two dimensional flow velocity vector.
u_m	The reconstructed mth target flow field.
u_N	Velocity field as a matrix at a given time step.
u_x	Horizontal component of the velocity field.
u_y	Vertical component of the velocity field.
X	Gap spacing between two PV panels.
y_i	Matrix M's eigenvector.
α	Inclined angle of PV panels.
ϕ_i	Corresponding ith KMD mode.
μ_i	Matrix M's eigenvalue.
ν	Fluid's kinematic viscosity.
ρ	Air density

I. INTRODUCTION

In recent years, photovoltaic (PV) panels have attracted widespread attention worldwide due to their clean and renewable characteristics.[1–3] Large-scale PV power plants established in open areas, such as coastal PV farms, are inevitably exposed to high wind loads, leading to wind-induced damage to PV panels.[4–6] The wind load interference effects among PV panels are critical factors influencing structural stability, durability, and energy output.[7–9] Therefore, a thorough understanding of the interference effects is essential for optimizing the structural design and spatial layout of PV panels, enhancing their wind resistance, and extending their service life.

Existing studies have extensively explored the wind load interference effects on PV arrays under various parameters, including shape, tilt angle, wind direction angle, ground clearance, and spacing. Shademan *et al.*[10] found the interference effects can impact vortex formation and wind loads on PV panels via numerical simulations of PV panels. Warsido *et al.*[11] studied the wind load distribution of PV arrays with a 25° inclined angle using wind tunnel tests. They found the PV panels' pressure coefficients reduced along the rows in the downstream direction, with the greatest reduction in the second row. Kray and Markus[12] found that wind loads on PV panels located at the edge of the group are significantly higher than those in the interior. Xu *et al.*[8] pointed out that the gap spacing of PV panels significantly affects wind loads, while the ground clearance has minimal impact. Sauca *et al.*[13] also confirmed this conclusion using CFD simulations. Wind tunnel tests of a stand-alone curved panel and arrays were performed by Winkelmann *et al.*[14] They obtained similar conclusions as for flat panel PVs. Ma *et al.*[15] studied the variation of wind load with inclined angles on stand-alone and arrayed PV panels using wind tunnel experiments.

The above studies reveal the complexity of wind load interference effects under various PV parameters. However, existing research relies mainly on simplified linear models to analyze the wind load distribution of photovoltaic arrays, which overlook the influence of nonlinear components. Airflow regimes between adjacent PV panels are intricate and highly nonlinear due to interference effects. It is crucial to understand the nonlinear components for accurately predicting wind load distribution and effectively addressing the impact of complex flow dynamics on PV arrays. This requires advanced analytical techniques to identify and quantify the unsteady flow behavior patterns of fluid interactions.

Dynamic Modal Decomposition (DMD) is a widely adopted technique for analyzing and identifying the dynamic behavior of fluid flows.[16] It enables the rapid extraction of spatiotemporal features associated with coherent structures in complex flow fields, providing valuable insights into the underlying flow dynamics. By decomposing temporal data into oscillatory components, the DMD method generates dynamic modes that reveal the dominant frequencies and growth or decay rates of flow structures. This ensures temporal orthogonality while preserving critical phase-related information, such as amplitude and frequency content.[17] Application areas of DMD include flow around airfoils, jets, wakes, and shallow flows, demonstrating its ability to capture dominant flow dynamics and coherent structures.[18–23]

However, DMD is susceptible to noise when capturing higher-order dynamic features and handling nonlinear flows, making it challenging to ensure accuracy. To address this challenge, this paper introduces the high-order Koopman Mode Decomposition (HOKMD) method, which incorporates higher-order nonlinear terms and high-frequency components into the traditional DMD framework. The application of HOKMD to analyze the nonlinear interference effects of wind loads on PV panels effectively reduces noise interference in mode identification. HOKMD demonstrates superior stability in reconstructing flow structures with strong high-frequency and nonlinear disturbances compared to DMD, providing a more accurate representation of the spatiotemporal evolution of airflow between adjacent photovoltaic panels. To the best of our knowledge, no study reports a thorough analysis of the spatiotemporal evolution of airflow at different inclined angles and gaps using the HOKMD methodology.

Moreover, to better understand the fundamental physical mechanisms of flow around PV panels, studying flow at low Reynolds numbers ($Re < 200$) is more appropriate than at high Reynolds numbers ($Re > 200$). Because turbulent distortion can be avoided under low Reynolds number conditions, the flow characteristics and vortex shedding mechanism can be revealed more clearly.[24] Furthermore, due to the inherently two-dimensional nature of vortex shedding, the coherent structures observed in laminar and turbulent flows exhibit similar features.[19,25,26] This means that studying laminar flows can provide valuable insights into the complex vortex-shedding phenomena, which is crucial for understanding flow behavior.

Therefore, this paper conducts CFD investigations on wind loads of two tandem PV panels at $Re = 150$. The influence of gap spacing (X/L) and inclined angle (α) on the mean, fluctuating wind loads, power spectra, and airflow structure of two tandem PV panels is examined. Through HODMD analysis, nonlinear dynamic modes and frequency information in the complex airflow between PV panels are extracted. These modes reflect the main coherent structures and mutual interference mechanisms in turbulence. Parameters analysis provides a reference for controlling wind loads and vibrations caused by the complex airflow around PV panels. It helps to deeply understand the nonlinear interference effect of airflow between PV panels and accurately predict the wind load distribution. The results can guide diagnosing the health of PV panels to ensure a longer lifespan. The key contributions of this paper are as follows.

1. This study establishes detailed physical models for tandem PV panels using high-fidelity CFD simulations, revealing the intricate relationship between gap spacing and inclined angles on wind load distribution. The models provide a robust framework for capturing the influence of aerodynamic interference on PV arrays.
2. Through a comparative analysis of single and tandem PV panels, this research provides new insights into how the airflow behavior generated by the upstream panel impacts the downstream panel's wind load and flow field. The findings uncover critical aerodynamic interactions and their implications for PV panel stability and design.
3. A HOKMD-based method is proposed to accurately identify the spatiotemporal dynamic characteristics of the intricate nonlinear airflow in the gap of PV panels. The interaction law between wind and PV panels is discovered, and the basic features of the wind load interference mechanism are uncovered.

The remainder of this paper is organized as follows. Section II introduces the numerical methodology. Section III shows the validity of this numerical simulation. Section IV discusses the physical mechanisms of fluid forces and interference effects on PV panels through numerical results. Section V concludes this paper.

II. NUMERICAL METHODOLOGY

A. Details of numerical simulations

The governing equations used in the simulations are the incompressible Navier–Stokes equations. These equations are expressed as follows:

$$\nabla \cdot u = 0, \tag{1}$$

$$\frac{\partial u}{\partial t} = -(u \cdot \nabla)u - \nabla p + \frac{1}{Re}\nabla^2 u, \tag{2}$$

where the u is the two-dimensional (2D) flow velocity vector, and p is the fluid pressure. Equation (1) is the continuity equation ensuring incompressibility, while Eq. (2) is the momentum conservation equation. The Reynolds number, denoted by Re, $Re = uL'/\upsilon$, where L' represents the projected width of the panel perpendicular to the wind, υ represents the fluid's kinematic viscosity, and u is the uniform wind speed at the inlet. At $Re = 150$, the vortex shedding of PV panels behaves as a 2D state and does not show the instability found in three-dimensional (3D) flows[27] (as verified in Sec. III). Direct numerical simulation (DNS) is employed to solve the 2D Navier–Stokes equations, directly capturing all spatial and temporal turbulence scales without relying on predefined turbulence models.[28] The spatial scales correspond to the computational grid and range from the smallest dissipative scale to the integration scale. To achieve high accuracy and efficiency, the spectral/hp element method was adopted, which combines the adaptability of finite element meshes with the precision and fast convergence of spectral refinement.[29] This study employed a Galerkin-based high-order spectral element technique to solve the DNS equations. Flow patterns and forces were analyzed using the NEKTRA++/5.1.0 open-source high-order spectral element solver.[29–31]

Figure 1(a) exhibits the computational domain of incident uniform free flow through the tandem PV panels. Here, X denotes the relative panel spacing and L denotes the length of the panel. According to Yang *et al.*'s[32] analysis, the solar panel employed in this investigation is similar to a thin panel defined by a length-thickness ratio of 100 : 1. The inclined angles are $\alpha = 5° - 55°$ and the dimensionless gap distances are $X/L = 1.0 - 4.0$. The case of a single panel represents $X/L = \infty$. Based on the Architectural Institute of Japan (AIJ) guidelines, the height of the computational domain between the tops of the PV panels and the upper boundary was set at a length of 10 L to ensure that the influence of the upper boundary on the flow field is minimized.[33] This configuration is consistent with prior aerodynamic studies on PV panels.[8,34,35] The length from the velocity inlet to the leading edge of the upstream panel (UP) is set to 10 L. The total length of the computational domain is 31 L. The height of the downstream panel (DP) above the ground equals $G/L = 0.8$. In Fig. 1(a), u_x and u_y are the horizontal and vertical components of the velocity field, respectively. Regarding the setting of the computational domain, the Dirichlet boundary condition was applied at the computational domain's inlet and upper boundary with free-stream velocity "$u_x = 1$, $u_y = 0$" and zero normal gradients of pressure $\frac{\partial p}{\partial \vec{n}} = 0$. To study the interference effects of tandem PV panels, both the ground wall and tandem panels were assigned a homogeneous Dirichlet boundary condition for velocity $(u_x = 0; u_y = 0)$ and a Neumann boundary condition for pressure $(\frac{\partial p}{\partial \vec{n}} = 0)$. For the outlet boundary, the velocity was governed by a Neumann boundary condition with zero normal gradients $(\frac{\partial u_x}{\partial \vec{n}} = 0, \frac{\partial u_y}{\partial \vec{n}} = 0))$, while the pressure was set to a pressure-free boundary condition$(p = 0)$. The computational domain is partitioned into macroelements, with each element utilizing Pth-order modal expansion polynomials as spectral basis functions. Second-order time accuracy is achieved by employing a velocity modification technique and a three-step time-spitted approach.[36,37]

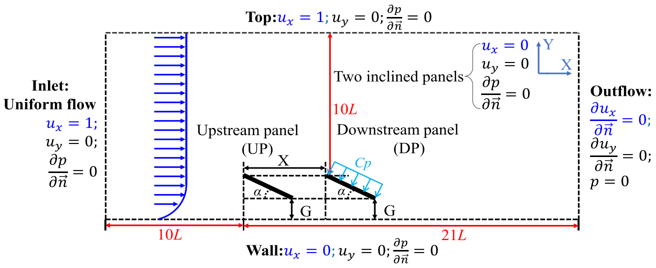

(a) Computational domain and boundary conditions of CFD.

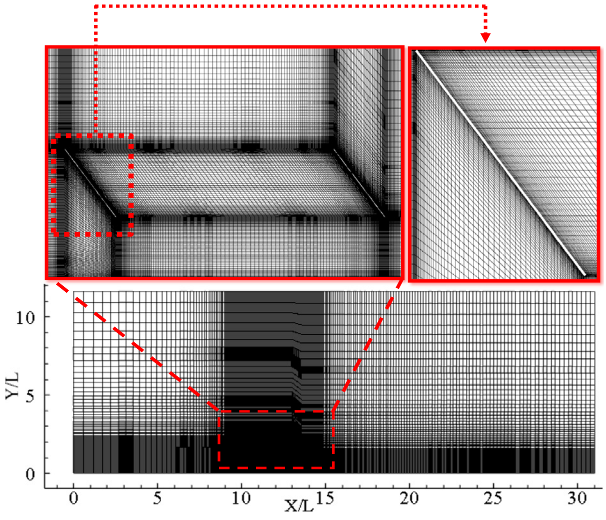

(b) Grid details.

FIG. 1. Numerically calculated flow domain configurations (a), global and local grid (b).

Figure 1(b) displays the grid scheme and a detailed enlarged view. The grid used for the numerical simulation is a quasi-structural grid designed by "Gmsh" which is an open-source software for the two-dimensional computational domain.[38] In this study, the mesh structure was carefully designed to ensure numerical accuracy and stability while minimizing computational cost. The grid spacing was determined based on a mesh convergence study, ensuring sufficient resolution to capture the flow field features, including vortex shedding and boundary layer development. Specifically, the grid spacing was refined near the tandem PV panels to resolve sharp gradients, while coarser spacing was employed in regions farther from the panels where flow variations are less significant. The grid scheme is identical to Foshat.[34]

Here, four simulated groups were used to verify the preliminary mesh, 30 simulated results were performed to investigate the fluid force properties, and 6 representative sampling results were used to examine the instantaneous flow regimes and to reveal the mechanism of interference effects.

To describe the frequency characteristics of the flow and to quantify the periodic behavior of vortex shedding, the Strouhal number was introduced with the expression $St = fL'/u$, where f is the vortex shedding frequency, $L' = L\sin(\alpha)$. The force coefficient of lift (Cl), drag (Cd), and pressure (Cp) on the panel are defined as

$$Cl = \frac{F_L}{0.5\rho u^2 L}, \tag{3}$$

$$Cd = \frac{F_d}{0.5\rho u^2 L}, \tag{4}$$

$$Cp = \frac{p - p_0}{0.5\rho u^2}, \tag{5}$$

where F_d and F_L represent the drag and lift of the panel per unit length (into the page). p_0 represents the static pressure. The Cp of the PV panel perpendicular and oriented to the panel surface is positive, as shown in Fig. 1(a). The grid details of the computational domain are shown in Fig. 1(b).

B. HOKMD technique

The data-driven dynamic model decomposition (DMD) technique, rooted in Koopman theory, offers a valuable approach for effectively modeling and linearly approximating complex, high-dimensional dynamics. Enhanced variants of the standard DMD, like HOKMD, excel in capturing essential features of intricate nonlinear turbulent flows. By augmenting the dimensionality of observable variables, HOKMD effectively handles dynamic behavior with misaligned time-space dimensions and noise interference, enabling accurate characterization of such behavior. Here, only general procedures are outlined; for a more comprehensive understanding of this method, readers are encouraged to refer to the study conducted by Wynn *et al.*[39]

Here, u_N represents the velocity field as a matrix at a given time step, with spatial grid points corresponding to the matrix dimensions and the matrix elements denoting the instantaneous velocity magnitudes. According to Koopman's assumption, the expression for transforming the snapshot image matrix u_{N-1} of the previous moment to the matrix u_N of the subsequent moment by incorporating the residual matrix R and the best-fitting linear mapping A is

$$Au_{N-1} = u_N + R, \tag{6}$$

$$u_{N-1} = [u_1, u_2, u_3, \ldots, u_{N-1}], \tag{7}$$

$$u_N = [u_2, u_3, u_4, \ldots, u_N]. \tag{8}$$

To discern the subspace with lower dimensions, the optimal problem is solved, i.e., the best mapping approximation is found by reducing the residual R. The optimization task can be framed as follows:

$$\min ||u_N - Au_{N-1}||^2 = \min \sum_{i=1}^{N} ||u_{i+1} - Au_i||_2^2, \tag{9}$$

$$\textit{such that } B^T B = I, M \in R^{r\times r}, B \in R^{q\times r}, \tag{10}$$

where r denotes the operator matrix's rank $A = BMB^T$, which is often less than q, and $||||_2$ represents the Frobenius matrix norm. In this scenario, incorporating low-order dynamics $A = BMB^T$ facilitates the estimation of the initial behavior. The following can be used to generate the rank-constraint expression in Eq. (9)

$$\min ||u_N - BMB^T u_{N-1}||^2, \tag{11}$$

$$M \in R^{r\times r}, B \in \left\{R^{q\times r} | B^T B = I, k < q\right\}. \tag{12}$$

Here, B stands for the subspace of lower dimensions, while M serves as a projection operator, providing a linear estimate of the evolution, and each series of B represents an orthogonal basis accounting for the eigenmodes' form. B and M are the two unknown matrices in Eq. (11). Resolving the minimization problem involving two variables is challenging. Additionally, this problem is nonconvex. The constraint $B^T B$ requires that the columns of B are orthonormal. Thus, B is optimal in Eq. (11) because it is the best r-dimensional subspace for elucidating the fluid dynamics of the snapshot data through a linear model.[39] Therefore, a decomposition of this rank constraint is known as Karman mode decomposition (KMD). As per Wynn *et al.*,[39] manifold flow optimization methods offer a solution to tackle the minimization problem. It is possible to rewrite the optimization problem as follows:

$$\max g(B) = ||B^T u_N Q(B)||^2, \tag{13}$$

$$B \in \left\{R^{q\times r} | B^T B = I, k < q\right\}, \tag{14}$$

$$Q(B) = u_{N-1}^T (B^T u_{N-1} B)^{-1} B^T u_{N-1}. \tag{15}$$

The ideal low-dimensional subspace sub-basis B_i and the associated space M are both achievable in the sense of least squares. The eigenvalue of KMD's logarithmic expression is

$$\mu_i = \frac{\log \sigma_i}{\Delta_t}, \tag{16}$$

where μ_i is the matrix M's eigenvalue. By providing a growth rate, the real component of μ_i can predict the stability over time, whereas the virtual component represents the ith mode's frequency. The dynamic model φ_i that is linked to the calculated value of μ_i is denoted by the following notation:

$$\varphi_i = By_i, \tag{17}$$

where y_i is the matrix M's eigenvector. The amplitude of the associated mode is represented by the projection parameter α_i

$$a_i = (\varphi^{-1})_{ij} (u_1)_j. \tag{18}$$

The energy E_i can be represented for each mode as the mode multiplied by its corresponding projection parameter

$$E_i = |a_i \varphi_i|. \tag{19}$$

The following method allows for the reconstruction of the mth original flow field (target flow field)

$$u_m = \sum_{i=1}^{n} a_i \varphi_i \lambda^{m-1}. \tag{20}$$

Here, u_m is a scalar of the flow field, which can represent the horizontal velocity component and the vertical velocity component. Nevertheless, the conventional KMD is insufficient for highly nonlinear cases, particularly when spectral and spatial complexity are regularly out of phase. Therefore, HOKMD is developed to complement the case of highly nonlinear flows. The foundation of HOKMD lies in Takens' delayed embedding theorem, thus enabling the augmentation of observed variable dimensionality.

Hence, using d index-lagged snapshots and the aid of HOKMD, the original observation matrix u_1^K is augmented to matrix $\bar{u}_1^{K-d+1}$ with a desired dimension as outlined in Eq. (22).

$\bar{u}_1^{K-d+1}$ is a submatrix made up of the adjusted snapshot matrix's initial $K-d$ and final $K-d$ columns. Then, the input data $\bar{u}_1^{K-d+1}$ is employed while the subsequent procedures are aligned with the standard KMD approach, termed HOKMD in the present study. Here, $\bar{u}_2^{K-d+1}$ represents u_N and $\bar{u}_1^{K-d+1}$ represents u_{N-1} in Eq. (9).

$$u_1^K = [u_1, u_2, \ldots, u_k, u_{k+1}, \ldots, u_{k-1}, u_k], \tag{21}$$

$$\bar{u}_1^{K-d+1} = \left[u_1^{K-d+1}, u_2^{K-d+2}, \ldots, u_{d-1}^{K-1}, u_d^K\right]^T, \tag{22}$$

$$\bar{u}_2^{K-d+1} = \left[u_2^{K-d+1}, u_3^{K-d+2}, \ldots, u_d^{K-1}, u_{d+1}^K\right]^T. \tag{23}$$

III. VERIFICATION AND VALIDATION

To determine the appropriate grid spacing and time step for the simulations, a thorough grid independence and time step independence evaluation was performed. This ensures that the simulation results are not influenced by the resolution of the computational domain or the size of the time step. Table I lists the results of the grid-independent and time step verification for two PV panels arranged in tandem ($\alpha = 25°$, $G/L = 1.0$, $X/L = 6.0$) at $Re = 150$. The Cl, Cl', and St of PV panels are compared using grids of low, moderate, and high resolution and at long, medium, and short time steps. The results demonstrate that as the polynomial order and time step resolution are refined, the aerodynamic parameters converge to stable values. Specifically, when $P\text{th} = 4$, the Cl and Cl' values of UP and DP change little compared to $P\text{th} = 3$, and both results converge. This confirms that the results are independent of the choice of grid and time step. In this study, a third-order resolution ($P\text{th} = 3$) grid and a time step of 0.0020 were selected to simulate the flow field of two tandem PV panels with different gaps and inclined angles to balance computational accuracy and efficiency.

Moreover, to verify the accuracy of the numerical simulations, the Cl and St of a single inclined panel ($X/L = \infty$) and two tandem PV panels are compared with previous studies, respectively. Table II shows the results of numerical results for PV panels. The minimal difference between the simulation results and those in the literature indicates the reliability and accuracy of the current simulation methodology.[35,40]

TABLE I. Grid and time step independence evaluation for two tandem PV panels ($\alpha = 25°$, $G/L = 1.0$, $X/L = 6.0$, $Re = 150$).

Pth-order	Time-step	C_l(UP)	C_l'(DP)	S_t
2	0.0025	0.976	0.544	0.131
3	0.0020	0.985	0.542	0.131
4	0.0015	0.986	0.541	0.131

In general, at the low Re, the flow's vortex shedding typically exhibits a two-dimensional condition and does not experience instability in three-dimensional flow. To further confirm this premise's validity, a case of 3D tandem inclined panels at $Re = 150$ ($\alpha = 25°$, $X/L = 6.0$) is simulated here by the DNS method. In the 3D case, the panel's spanwise length is given as 2π, which is similar to the normal panel dimensions of Najjar and Balachandar[41] and Yang *et al.*[32] for $Re = 250$ and $Re = 1000$, respectively. In the simulation, the Fourier expansion form is employed to model the flow motion in the z-direction. Here, the aggregate spanwise length of the Fourier planes amounts to 48, equivalent to utilizing 48 grid cells along the spanwise direction in the finite element approach. The grid setup parameters in this study are the same as those of Najjar and Vanka.[42] The simulation results of the PV panels in 2D and 3D are presented in Table III. By comparing the lift coefficients of the panels, it was found that there is a negligible disparity between the results of the 2D and 3D simulations. It indicates there is no occurrence of 3D instability in vortex shedding at $Re = 150$. Two-dimensional numerical simulation can well reveal the vortex shedding pattern of the PV panel's flow field. Therefore, in this study, 2D numerical simulation is employed to investigate the aerodynamic characteristics of two tandem PV panels to improve the computational efficiency and save computational cost.

IV. RESULT AND DISCUSSION

A. Wind load property

Figure 2 displays the variation of the mean and root mean square (RMS, denotes fluctuating) drag forces of UP and DP with the dimensionless panel spacing (X/L) and the panel inclined angle (α). The drag forces of two tandemly arranged panels are contrasted with those of the single inclined panel (considered to be spaced at infinity). Generally, the tendency of the mean and RMS drag coefficients of UP and DP to vary with the panel inclination is different. For the UP, the mean drag force applied to UP closely resembles that of a single panel for all intervals at $\alpha < 25°$. As the α increases, the mean drag force on UP for all gap spacing cases is gradually smaller than that of the single panel, suggesting a gradual enhancement of the interference effect of the DP on the UP. Moreover, at small spacings ($X/L \leq 2$), as depicted in Fig. 2(a), the RMS drag forces of UP are significantly less than that at large spacings ($X/L > 2$) with $\alpha > 25°$. This suggests the presence of DP reduces the UP's RMS drag force at small spacings.

For the DP, there is a considerable reduction in the mean drag force of DP compared to the single panels, which is due to the shielding effect of UP. The shielding effect of UP on DP varies with X/L and α. For the small spacings ($X/L \leq 2$), the mean drag of DP is less than that of large spacings. It indicates that the shielding effect of UP on DP is stronger at small spacings than at large ones. Furthermore, it can be observed from Fig. 2(d) that the RMS drag of DP grows progressively with the increase in α. Especially at $X/L > 2$, the large α significantly increases the RMS drag of the DP compared to that of the single panel, which means the flow field of DP becomes more complex.

Figure 3 shows the variation of the mean and fluctuating (RMS) lift forces of UP and DP with the dimensionless panel spacing (X/L) and the panel inclined angle (α). It can be seen from Figs. 3(a) and 3(c) that the mean lift of both tandem panels is less than that of the single panels. This indicates that the interference effect existing between two

TABLE II. Validation of numerical results for PV panels.

	Re	α	X/L	G/L	*Cl* (UP)	*Cl* (DP)	*St*
Current study	300	20°	∞	1.0	0.927	…	0.161
Li *et al.*[40]	300	20°	∞	1.0	0.926 (0.1%)	…	0.160 (0.63%)
Ai *et al.*[35]	300	20°	∞	1.0	0.927	…	0.161
Current study	150	25°	6.0	1.0	0.955	0.543	0.131
Ai *et al.*[35]	150	25°	6.0	1.0	0.956 (0.1%)	0.542 (0.18%)	0.131

tandemly arranged panels suppresses the mean lift force. For the UP, as α increases, the lift of the UP gradually increases. Moreover, in Fig. 3(c), the RMS of UP's lift is close to 0 when $\alpha < 35°$ for the small spacings ($X/L \leq 2$), which indicates that the flow between two inclined panels is in a steady state. Interestingly, the flow between two panels becomes unstable when $\alpha \geq 35°$. Moreover, the RMS lift values of the UP at $X/L > 2$ are similar to those of the single panels, and the shedding of the vortex gradually strengthens as α increases.

Compared with Figs. 3(b) and 3(d), the mean lift of DP is smaller than that of UP at all X/L, as a result of the shielding effect provided by UP. The RMS lift force of the DP exhibits two features under the interference effect. It is clear from Fig. 3(d) that the RMS value of DP at large spacing ($X/L > 2$) is almost always larger than that of the single panel when $\alpha > 15°$, however, the opposite is achieved for small spacing ($X/L \leq 2$). Thus, two features can be described as the shielding effect of UP on the fluctuation lift of DP at small spacing and the amplification effect at large spacing. Furthermore, the maximum RMS lift of DP appears at $\alpha = 35°$. This suggests that the flow field state in this instance is incredibly unstable and the vortex shedding intensity of DP is strongest.

B. Power spectrum density of the fluctuating lift force

Figure 4 shows the power spectrum density (PSD) of the fluctuating lift for the single PV panels and two tandemly arranged panels with $X/L = 2$ and 3 for three representative cases of $\alpha = 25°$, 35°, 55°. The effect of the inclined angle of the panel and the interference effect on the frequency domain characteristics of the flow field is studied by comparing the results of both UP and DP and a single panel. In Fig. 4, the power spectrum exhibits a multipeak pattern in all cases. The peak of the fluctuating lift force's PSD changes significantly with the change of α. Therefore, the inclined angle is a crucial factor affecting the PV panel's vortex-shedding frequency. Moreover, the frequency of the spectrum peak increases multiply, which implies that the instability of the flow around the inclined panel is influenced by the vortex motion, the flow regime, and the nonlinear factors in the flow field. For a single panel, as shown in Fig. 4(a), the dominant frequency and the corresponding peak increase gradually as α increases (from 0.126 to 0.176). This indicates that the vortices adjacent to the PV panel in the flow field develop from low-energy large-scale vortices to high-energy small-scale vortices as the inclined angle increases.

TABLE III. Fluid forces of two tandemly arranged panels obtained from both 2D and 3D simulations.

Case	C_l(DP)	C_l(UP)	C_l'(DP)	C_l'(UP)
2D simulation	0.8013	1.0774	0.6370	0.0528
3D simulation	0.8011	1.0774	0.6371	0.0529

When two inclined panels are arranged in tandem, it is observed that the spectral peaks of UP and DP have the same frequency, indicating that the two panels' vortices are shed at the same frequency. However, the higher spectral peak of the DP compared to that of the UP indicates a stronger vortex-shedding intensity of the DP, which results in a larger lift force on the DP. In Fig. 4(b), no fluctuation in the lift forces of UP and DP with time is observed at $\alpha = 25°$, $X/L = 2.0$, thus, the flow field is in a steady state and the power spectrum is not demonstrated here. For two panels with the gap spacing of $X/L = 3.0$, it is found by comparison that the predominant peak frequency gradually increases with increasing α, which is similar to the phenomenon of a single panel. By comparing the power spectrum at a given inclined angle, it is found the interference effect of two tandem panels exhibits the following two phenomena: (i) For $X/L = 2.0$ and 3.0, the dominant peak frequency of two tandem panels is significantly decreased when DP is arranged behind the single panel. (ii) As the inclined angle increases, the interference effect becomes progressively stronger, which is manifested as the difference between the peak frequencies of UP and DP becomes larger (from $\Delta St = 0.03$ to $\Delta St = 0.08$) as shown in Figs. 4(c) and 4(d).

C. Instantaneous flow structure

The fully developed state of the flow is characterized by the time history of the pressure coefficient reaching a periodic and stable oscillation pattern. Figure 5 shows the pressure coefficient of DP for $X/L = 3.0$ and $\alpha = 25°$. The pressure coefficient shows periodic convergence, with the variation between consecutive cycles less than 0.1%. All subsequent analysis of the flow field was performed only after confirming the steady-state behavior of all configurations to ensure the reliability and consistency of the results.

The flow vortex structure around the panel is obtained based on the flow velocity extracted from the snapshot. To investigate the influence of the inclined angle on the flow field of the PV panels, Fig. 6 shows the instantaneous vorticity field in three representative scenarios with $X/L = 3.0$ and $\alpha = 25°$, 35°, and 55° for the single and two tandem panels. In Fig. 6, the area of vortex formation is considered as the vortex strength, and the pink and green vortices dominate the flow past the panel, respectively. Moreover, the vortex structure of the wake in Fig. 6(a) is to the findings of Yang *et al.* (2012).

In general, the inclined angle influences the flow structure of the panel, albeit all of them exhibit the vortex shedding phenomenon. For the single panel, two counter-rotating vortices are observed at the leading and trailing edges, which implies the panel is exposed to the

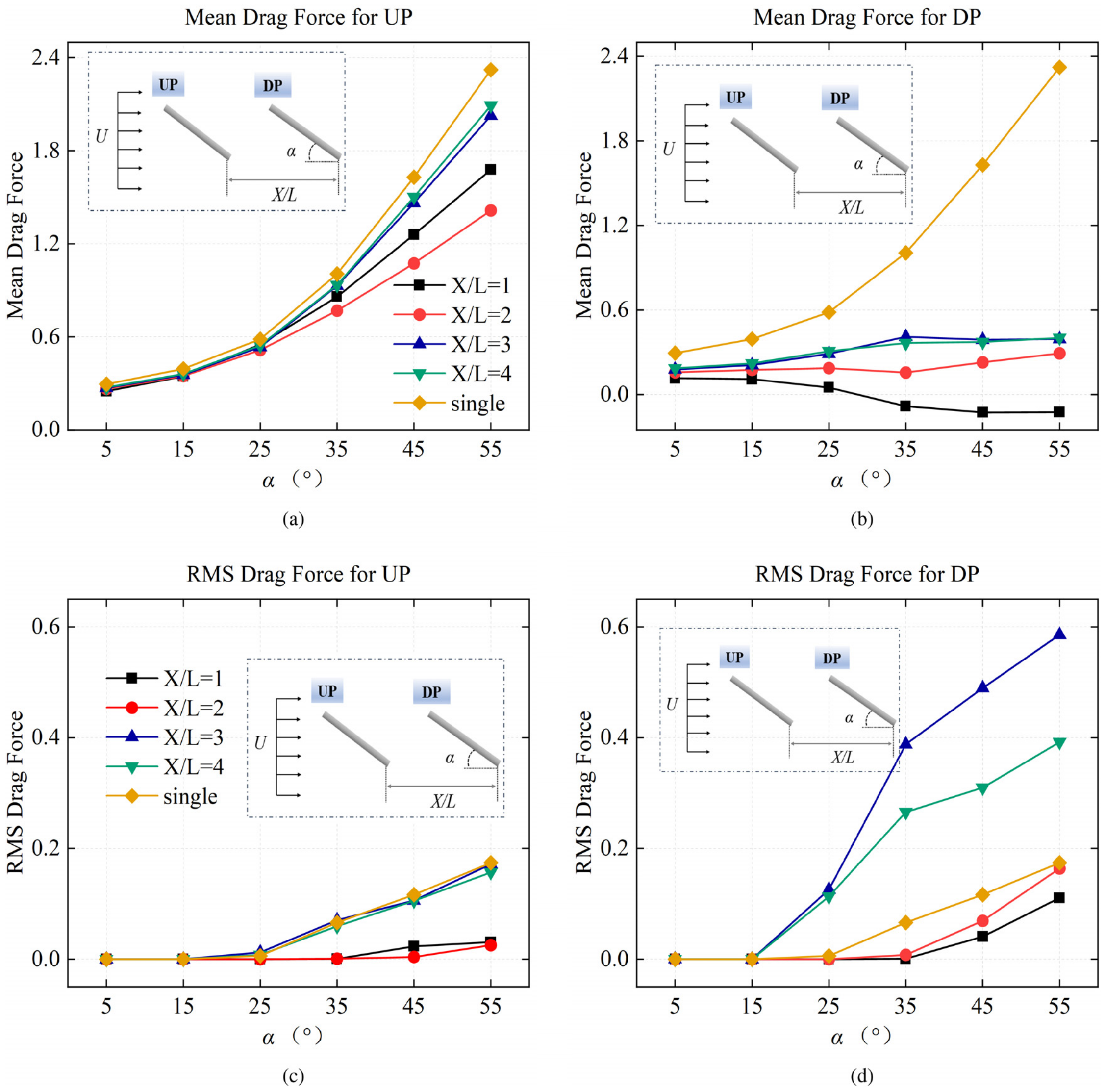

(a) (b)

(c) (d)

FIG. 2. Variation of mean drag force and root mean square (RMS) drag force for UP and DP as a function of panel spacing X/L and inclined angle α.

fluctuating load. As the α increases, the intensity of the vortex shedding becomes stronger behind the panel, and its wake gets longer, indicating that the panel's load gradually increases. Also, it is seen that as the inclined angle increases, the vortices shedding from the leading and trailing edges of the panel gradually expand their paths.

Compared to a single inclined panel, an interference effect is observed between two tandem inclined panels in Fig. 6. In Fig. 6(b), the free flow passes over the UP before the DP, which reduces the fluid force on the DP and provides a shielding effect. In addition, since the DP is submerged in the wake of the UP, the vortices formed and shed from the leading and trailing edges of the UP continuously slap the DP, which increases the fluctuating force and augments the flow instability of the DP. As the α increases to 35°, the vortex shedding of the UP strengthens, thus, the fluid force instability of the DP increases. Interestingly, when the α increases to 55°, the vortex shedding from the leading edge of the UP bypasses the DP due to the wide wake of the UP, which significantly reduces the force fluctuation of the DP. It explains the drop portion of Fig. 3(d) in the large inclination range. Additionally, because of the obstruction effect of DP, the counterclockwise vortex shedding from the trailing edge of the UP is constrained, which reduces the lift force of UP.

D. Coherent structure and mode analysis

Investigating the flow evolution around the PV panel and the formation of coherent structures from the perspective of the flow field contributes to unraveling the underlying mechanisms of interference effects. From the above discussion, it is evident that aerodynamic characteristics of PV panels are highly sensitive to changes in inclined angles. Therefore, this section employs HOKMD to analyze data for

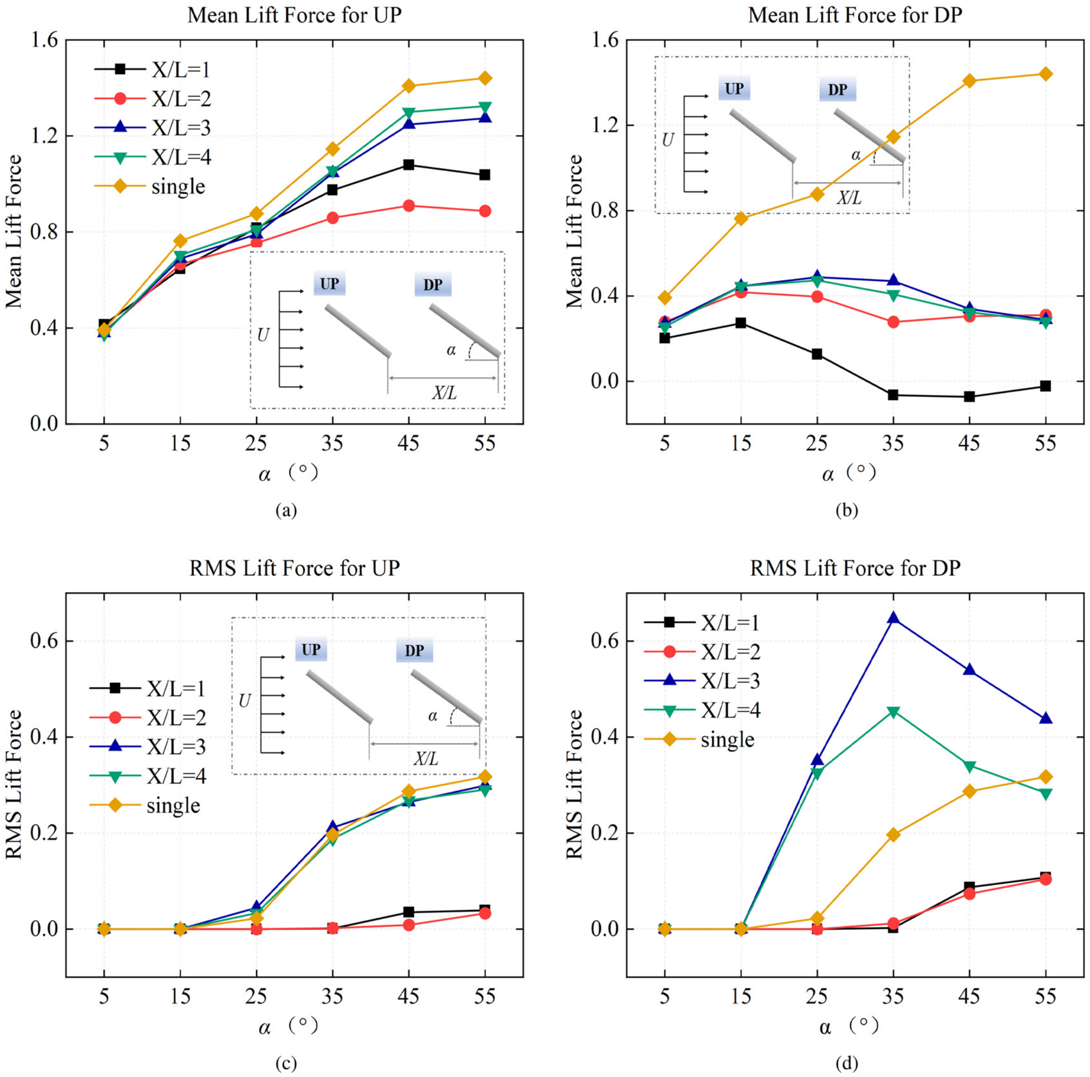

FIG. 3. Variation of mean lift force and root mean square (RMS) lift force for UP and DP as a function of panel spacing X/L and inclined angle α.

three typical inclined angles, aiming to explore the spatiotemporal characteristics of vortex structures hidden in the flow field. (1) Ritz value μ, as a complex number expressed in Eq. (16), represents the eigenvalue spectrum through its real and imaginary portions (i.e., location of the mode points). The flow pattern either diverges or decays with time, depending on whether the mode points are on or off the unit circle. The mode points on the unit circle imply the occurrence of limit cycle oscillation in the associated fluid mode. If the data are acquired from a fully developed flow field, the μ for the main vortex coherent mode is supposed to fall on the unit circle. (2) φ_i, denotes coherent mode structure morphology, expressed by Eq. (17). (3) E_i, as written in Eq. (19), denotes the mode turbulence energy and enables to quantify the mode's contribution to the flow field.

Before carrying out HOKMD, verification tests are required for the main impact parameters, such as embedding number, sampling frequency, and duration. The precise implementation procedure is displayed in our earlier investigations,[43] thus, is not presented here. In the fully developed flow field, the snapshot acquisition time is 40 vortex shedding periods and the time interval is taken as $1/20$ of the period, following the sampling theorem. Additionally, the modal points almost always fall on the unit circle when the embedding value $d > 4$, demonstrating that the flow field is essentially steady.

Figure 7 shows the distribution of the Ritz values for the decomposition of the mode on the unit circle using the HOKMD technique for $\alpha = 25^\circ, 35^\circ$, and 55° at $X/L = 3.0$, respectively. In the figure, the color bar on the right side indicates the mode energy. The dominant modes for the three α are almost spread over the unit circle as anticipated. Moreover, the points of other modes are almost on the unit circle. It demonstrates the reliability of the modal extraction results. Furthermore, to determine the relationship between the flow regime and the fluid forces on the PV panels, a profound analysis of the velocity and pressure fields of the panel's modes is performed with the

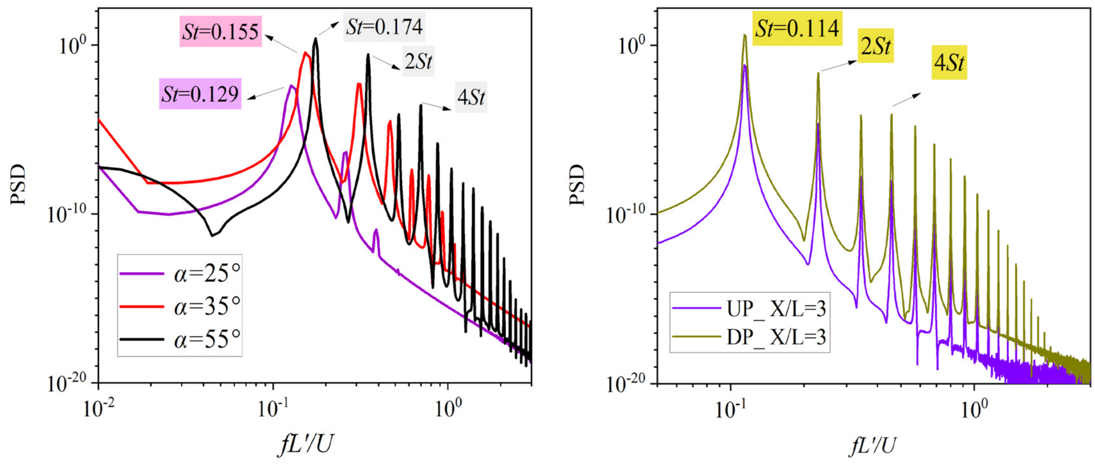

(a) single PV panel

(b) $\alpha = 25°$

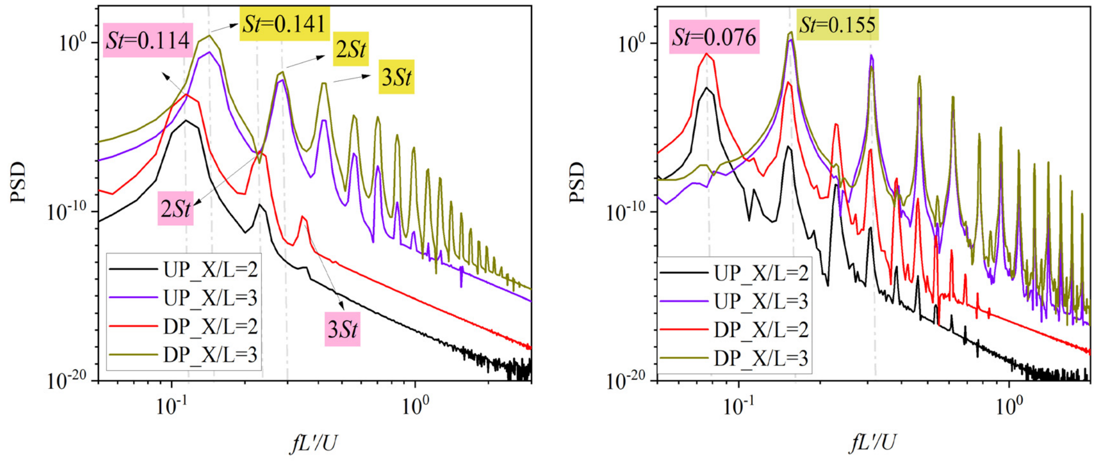

(c) $\alpha = 35°$

(d) $\alpha = 55°$

FIG. 4. Variation of fluctuating lift PSD for single and tandem panels at different inclined angles.

HOKMD method. To further explore the interference effects of PV panels, mode maps of the single panel are also provided here for comparison.

1. α=25°

Figure 8 shows the mode energy spectrum of the single panel and two tandem inclined panels at $\alpha = 25°$. In Fig. 8, it is evident that the mode energy is highest at $fD/U = 0$, which indicates the contribution of the mean flow mode. In addition, the primary harmonic mode (M1) and superharmonic mode (M2) are obtained with substantially lower energy than that of the mean flow mode, which implies the contribution of the dynamic mode. Since the energy of M1 and M2 are higher than the other modes, the flow regimes of M1 and M2 could represent the main dynamic modes in the flow field. In Fig. 8(a), the peak of the primary harmonic mode appears at $fD/U = 0.129$, which corresponds precisely to half of the superharmonic mode ($fD/U = 0.258$).

When two inclined panels are arranged in tandem, the energy and the dimensionless frequency of the first- and second-order modes are significantly decreased. This suggests that the interference effect between the panels lessens the nonlinearity of the dynamics. Also, an increase in the mean flow mode energy is seen in Fig. 8(b), which indicates that the interference effect stabilizes the flow field to some extent and reduces the wind load fluctuations on the panels.

Figure 9 shows the first two orders of vorticity modes (M1 and M2) with velocity streamlines for the single and two tandem inclined panels. Figure 10 shows the first two orders of pressure mode contour diagrams for the single and two tandem inclined panels. Moreover, to quantitatively study the pressure variation on the surface of the PV panel, the modal pressure coefficients on the up and down panel's surfaces are presented in Fig. 11. Here, S/L stands for the dimensionless distance from the leading edge.

For the single panel, the vortex alternating shedding at the trailing edge with a 2S wake pattern is seen in Fig. 9(a), which contributes to the fluid force. From the second-order vorticity mode in Fig. 9(c),

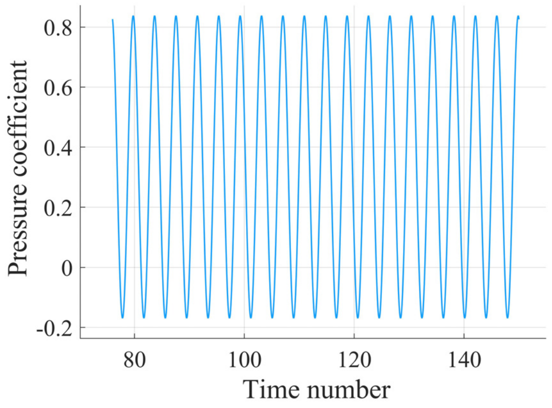

FIG. 5. Pressure coefficient time-history spectrum for DP at $X/L = 3$ and $\alpha = 25^\circ$.

relatively small vortex structures are uncovered in the flow field. For the two tandem panels, it is clear from Fig. 9(b) that two high-energy vortices with opposite rotation directions are in the gap. As the flow develops downstream, the DP divides the gap vortex, and subsequently, the gap vortices merge with the wake vortex of the DP. This causes the upper and lower surfaces of the DP to be subjected to strong reverse pressure, as shown in Fig. 10(b), which imposes a lift force on the DP as a whole. In addition, few vortex structures are observed around the UP, so the pressure on the UP is very small compared to that of the DP. As shown in Fig. 9(d), for the second-order mode, the small vortex structure in the gap first collides with the leading edge of the DP as it moves downstream, which results in a higher pressure in the wake flow at the leading edge than at the trailing edge. This explains why the pressure coefficient in Fig. 11(d) for $S/L < 0.5$ is larger than that for $S/L > 0.5$.

2. α=35°

The mode energy spectra of the single and tandemly arranged panels with 35° inclined angle are shown in Fig. 12. Compared with $\alpha = 25^\circ$, the frequency and energy of the first two order modes of the single and two tandem panels at $\alpha = 35^\circ$ are significantly increased. It implies stronger vortex shedding and a more complex flow field. Figures 13 and 14 show the flow field from the perspective of the vortex and pressure modes, respectively. The corresponding pressure mode coefficients on the surface of UP and DP are shown in Fig. 15.

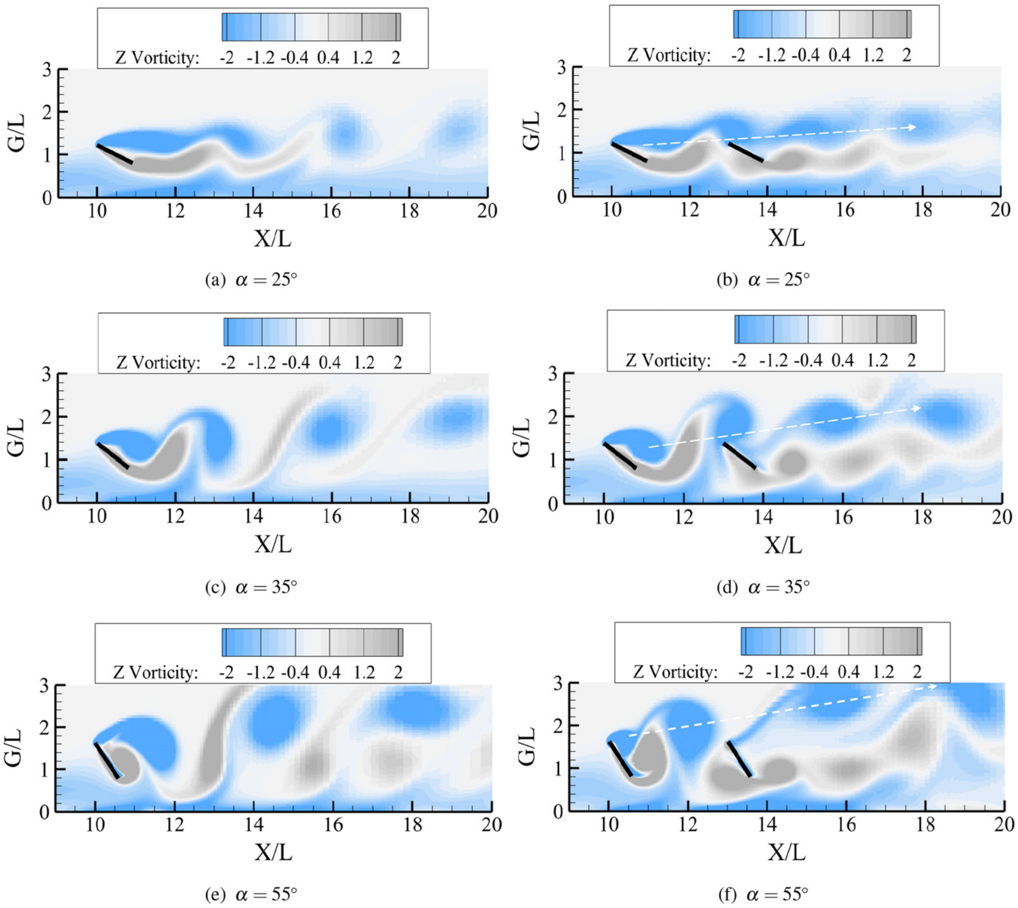

(a) $\alpha = 25^\circ$ (b) $\alpha = 25^\circ$

(c) $\alpha = 35^\circ$ (d) $\alpha = 35^\circ$

(e) $\alpha = 55^\circ$ (f) $\alpha = 55^\circ$

FIG. 6. Instantaneous vorticity maps of the single panel (a) and two tandem panels ($X/L = 3.0$) (b) at $\alpha = 25^\circ, 35^\circ, 55^\circ$.

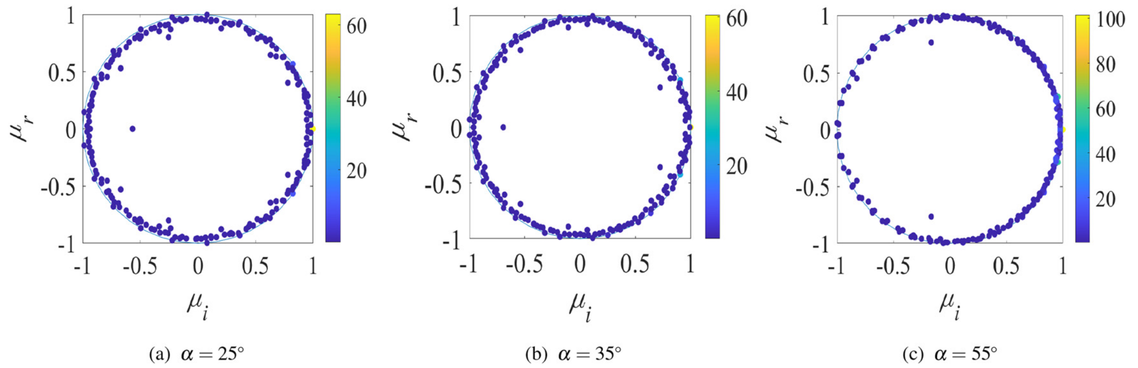

(a) $\alpha = 25°$ (b) $\alpha = 35°$ (c) $\alpha = 55°$

FIG. 7. Distribution of Ritz values on the unit circle for two tandem inclined panels ($X/L = 3.0$) at $\alpha = 25°, 35°, 55°$.

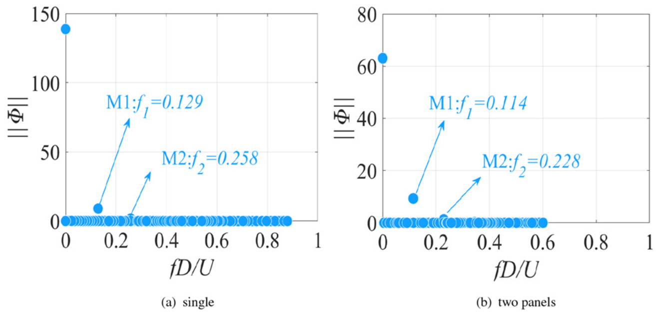

(a) single (b) two panels

FIG. 8. Comparison of mode energy spectra of single (a) and tandem inclined panels (b) at $\alpha = 25°$.

In Fig. 13(a), no vortex is found on the windward of the single panel while the leeward exhibits a 2S vortex pattern. The fluctuating force applied on the panel is caused by the separation bubbles on the up-surface of the panel. For the second-order mode, two distinct clusters of small-scale vortices are observed in the wake of the single panel in Fig. 13(b), which then merge into large-scale vortices in the far wake region. When two PV panels are arranged in tandem, many small irregular vortices are observed in the gap and far wake in Fig. 13(d). It indicates the increase in fluctuation energy at high frequency in the flow field. The impact of gap vortices on the UP is relatively minor, leading to a smoother pressure distribution along the leading-to-trailing edge of the UP compared to a single panel. The fluid force on the UP at larger gaps ($X/L > 2$) aligns closely with that observed for a single panel, which explains Figs. 2(c) and 3(c). Compared to the vorticity

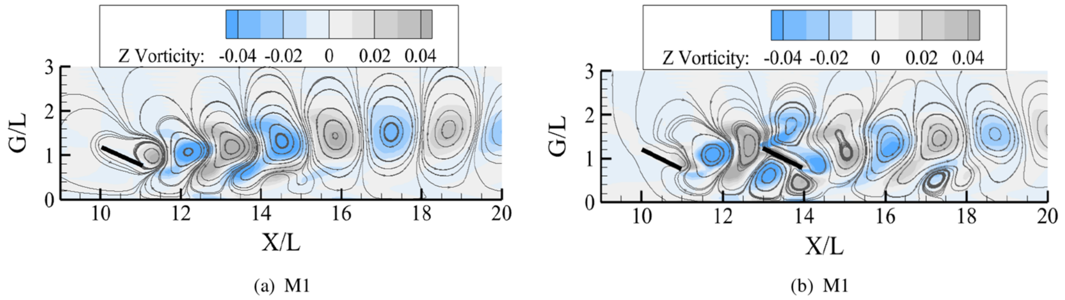

(a) M1 (b) M1

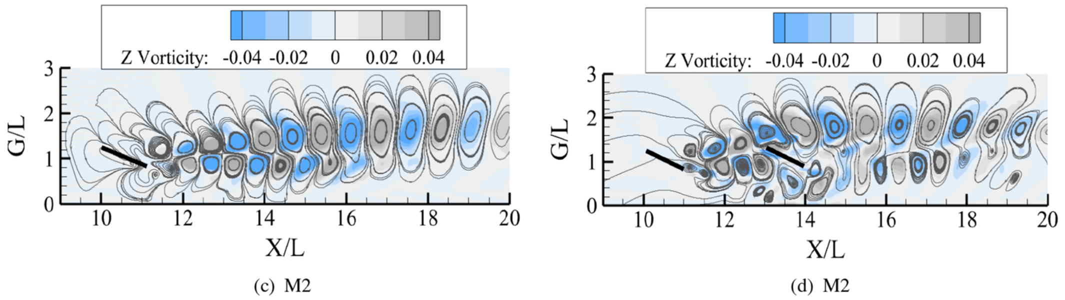

(c) M2 (d) M2

FIG. 9. Vorticity modes of the first two orders for the single panel (a), (c) and two tandem inclined panels (b), (d) at $\alpha = 25°$.

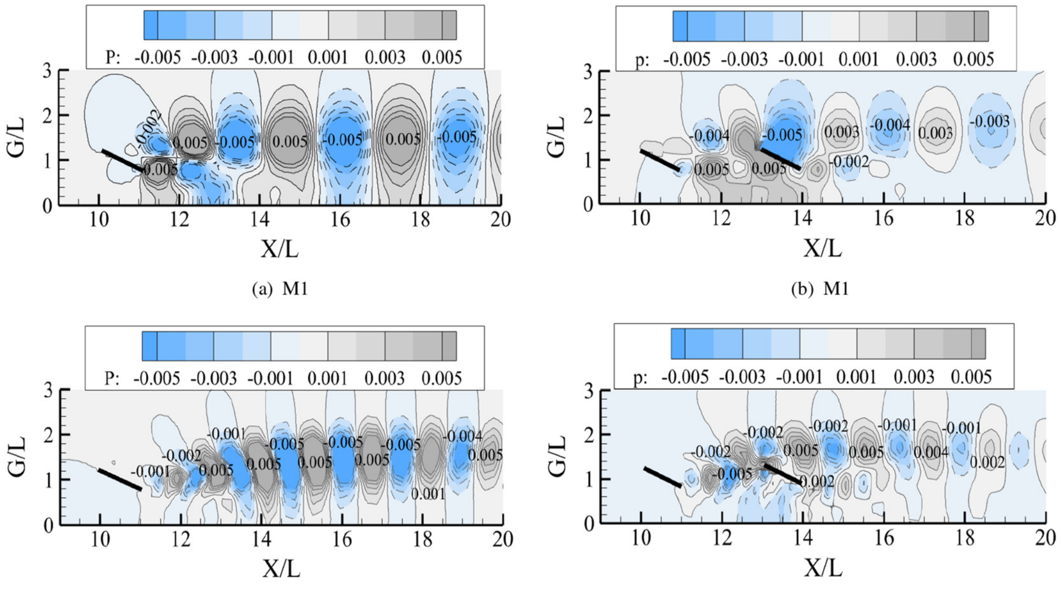

(a) M1

(b) M1

(c) M2

(d) M2

FIG. 10. Pressure modes of the first two orders for the single panel (a), (c) and two tandem inclined panels (b), (d) at $\alpha = 25°$.

in M2 at $\alpha = 25°$ and 35°, compared to the vorticity of $\alpha = 25°$ and 35°, it is found that the small-scale gap flows and pressure become stronger in M2, and the change of the large-scale vortex in M1 is not obvious. The small-scale gap flow increases the pressure fluctuations on the up-surface of UP and the down-surface of DP as shown in Fig. 15(d).

3. α*=55°*

Figure 16 displays the mode energy spectra of the single and tandem PV panels with $\alpha = 55°$. Compared with the single panel case, the dominant frequency of the first-order mode of two tandem panels is smaller and accompanied by higher energy. It reveals an increase in low-frequency large-scale vortices with high energy in the flow field. Moreover, it is obvious that many superharmonic modes appear in the low frequency, yet the peak is not significant. Therefore, the main focus is on the morphology of the first-order dominant modes.

Figures 17 and 18 show the vorticity and pressure fields of the first-order modes, respectively. The quantitative pressure modal coefficients of the panel surface are depicted in Fig. 19. For a single panel, as α increases, the path of vortex shedding shows an upward tilt, which is also known as jet flow. Therefore, the vortex shedding behind the panel moves closer to the windward leading edge of the up-surface. In addition, for M2 of the single panel, the increase in α makes the pressure on the windward leading edge and trailing edge of the panel gradually increase. This is due to the increase in α accelerates the airflow at the leading edge and creates a stronger separation effect at the trailing edge.

For the tandem panels, the jet tendency is considerably evident. Due to the jet flow, the large-scale vortex shedding from the UP bypasses the DP, while suppressing the vortex shedding from the DP, as shown in Fig. 17(b). Therefore, the up-surface pressure of DP is almost zero and the DP's fluctuating lift is the contribution of the gap vortex in Fig. 19(b). This indicates that the DP panel is more susceptible to the vortex shedding path from the UP panel, and thus, the DP is more sensitive to changes in inclined angle.

V. CONCLUSION

In this paper, the effect of inclined angle and gap spacing on flow past two PV panels arranged in tandem is investigated by numerical simulation. The gap spacing between the two panels ranges from $X/L = 1.0$ to 4.0 with an interval of 1.0, and the inclined angle (α) ranges from 5° to 55° with an interval of 5°, and the ground clearance is $0.8\,L$. Accordingly, the variation patterns of fluid forces, power spectra, and vorticity fields of single and two tandem PV panels were analyzed. To explore the intrinsic mechanism of the effect of the inclined angle on the interference effect, three representative cases, i.e., velocity and pressure fields with $X/L = 3.0$, $\alpha = 25°, 35°$, and 55° were analyzed simultaneously by HOKMD. The temporal-spatial attributes of the coherent vortex structure were captured and the correlation between the fluid forces and flow pattern was further elaborated.

1. In general, there is a significant interference effect between two tandem inclined panels, and such interference effect strongly depends on the inclined angle and spacing of the panels. At $\alpha > 25°$ and $X/L \leq 2.0$, the interference effect of two tandem PV panels is more pronounced, as evidenced by the reduction in the coefficient of fluid forces on mean and fluctuations. At large panels' spacing ($X/L > 2.0$), the shielding effect of UP has a significant effect on the fluid force of DP, specifically in the form of suppression of the mean drag force and amplification of the fluctuating lift force. The amplification effect on the fluctuating force of DP is strongest at the gap spacing of $X/L = 3.0$ and an inclination of $\alpha = 35°$.

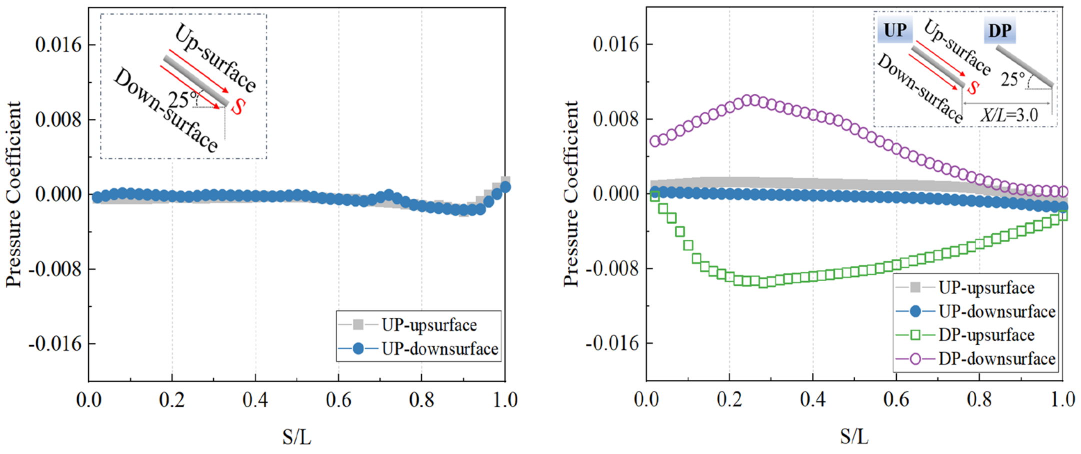

(a) M1 (b) M1

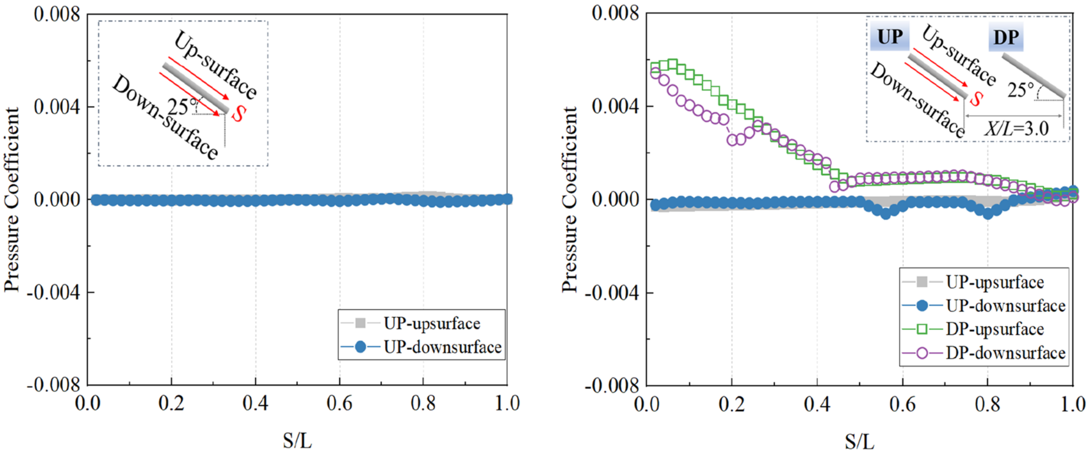

(c) M2 (d) M2

FIG. 11. UP and DP surface pressure distributions for single (a), (c) and two tandem panels (b), (d) at $\alpha = 25^{\circ}$.

2. For a single inclined panel, the predominant frequency and the peak increase correspondingly with increasing inclination, resulting from the development of high-energy small-scale vortices adjacent to the PV panel confirmed by the super-harmonic DMD mode. Moreover, as the inclined angle increases, the intensity of vortex shedding behind the panel increases and the wake of the panel is elongated, which induces higher fluid forces on the panel. For two PV panels arranged in tandem, the vortex shedding frequency is the same for UP and DP, but the vortex shedding strength is stronger for DP. The reason for this is that the DP is submerged in the wake of the UP, and the vortex formed by the leading and trailing edges of the UP continuously slaps the DP, which increases the fluctuating force of the DP and enhances the flow instability. As a result, the PV panels on the rear side are more vulnerable to wind-related vibrations brought on by vortex shedding.

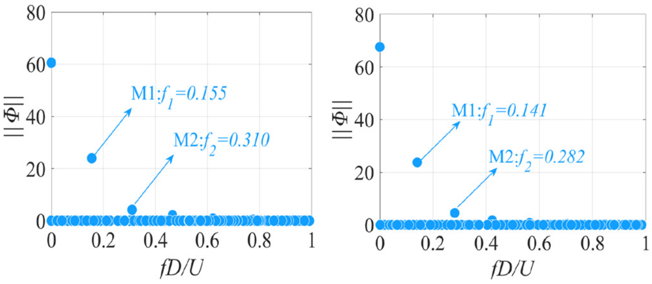

(a) single (b) Two panels

FIG. 12. Comparison of mode energy spectra of single (a) and tandem inclined panels (b) at $\alpha = 35^{\circ}$.

3. The temporal and spatial evolution properties of the dominant mode coherent structure with different inclined angles are explored by the HOKMD technique, and the interference effect's fundamental mechanisms of inclined angles around PV panels are revealed. Overall, two dominant dynamic modes are captured by HOKMD, i.e., primary harmonic mode (M1) and superharmonic mode (M2), and the energy of M1 is higher than that

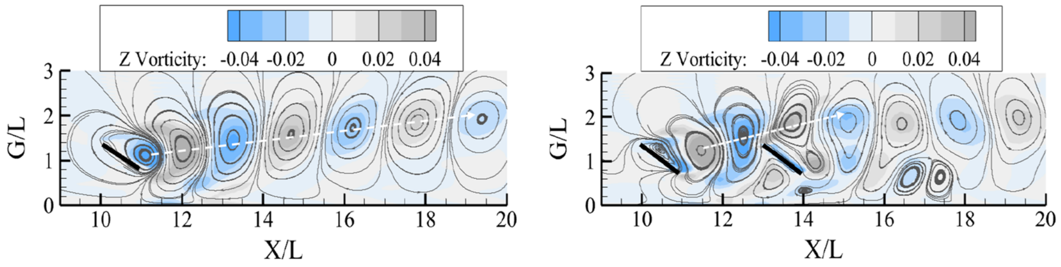

(a) M1 (b) M1

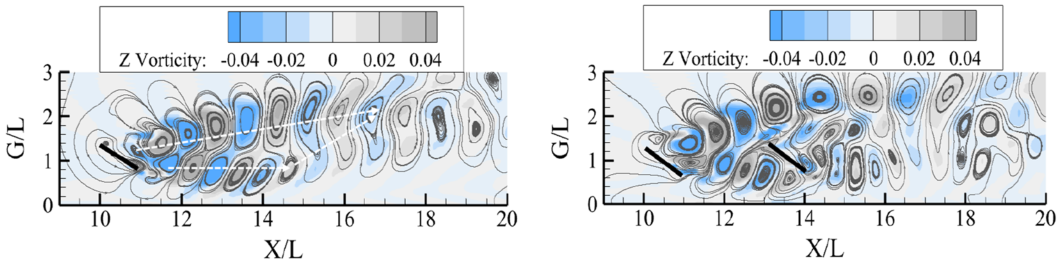

(c) M2 (d) M2

FIG. 13. Vorticity modes of the first two orders for the single panel (a), (c) and two tandem inclined panels (b), (d) at $\alpha = 35^{\circ}$.

of M2. For a single PV panel, the primary flow mode exhibits alternating shedding vortices with a 2S pattern in the wake, albeit no vortices are discovered on the up-surface. Thus, the fluctuating forces on the PV panel are caused by the continuously flowing separation of the vortices on the up-surface. Moreover, as the inclined angle increases, the path of vortex shedding shows an upward jet trend with enhanced intensity, meanwhile, the range of separated bubbles on the up-surface of the panel is gradually close to the windward leading edge. Therefore, the wind load enhancement on the windward leading edge of a single PV panel caused by the jet phenomenon should be considered when designing a single solar panel at a large inclined angle.

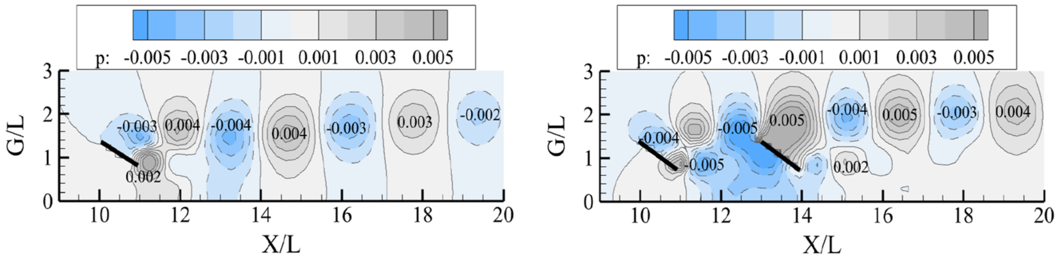

(a) M1 (b) M1

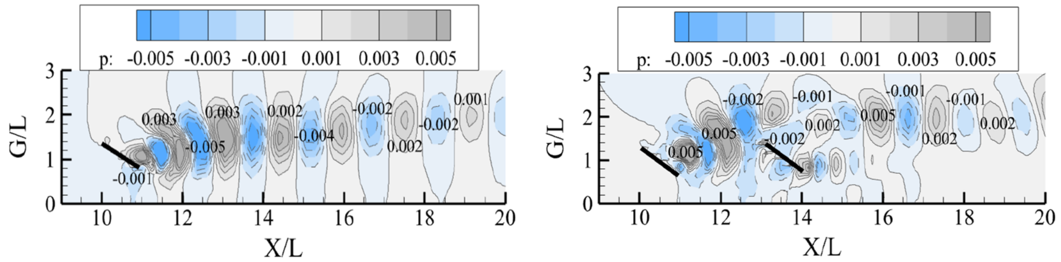

(c) M2 (d) M2

FIG. 14. Pressure modes of the first two orders for the single panel (a), (c) and two tandem inclined panels (b), (d) at $\alpha = 35^{\circ}$.

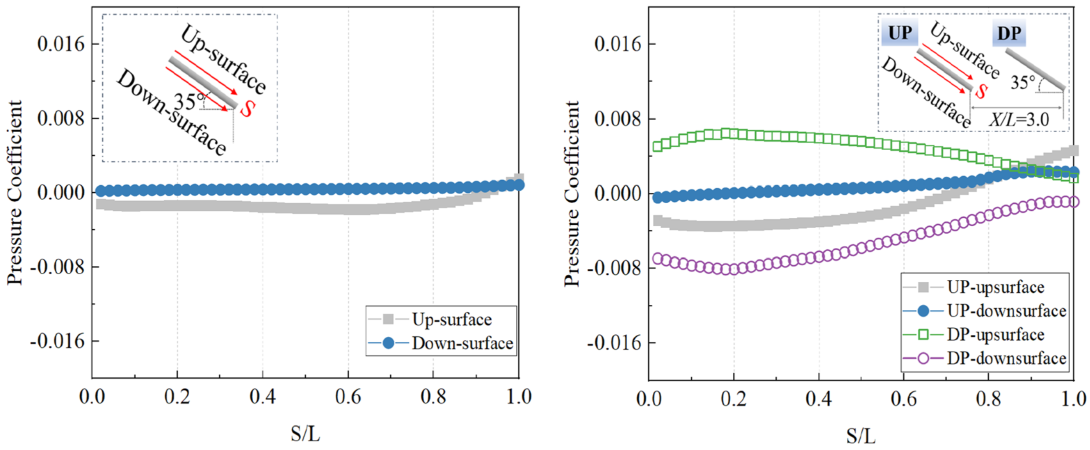

(a) M1 (b) M1

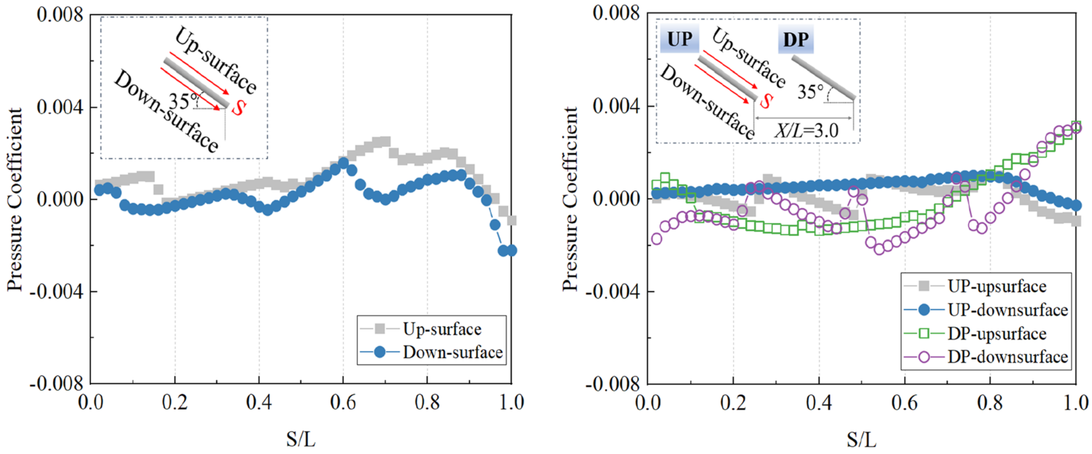

(c) M2 (d) M2

FIG. 15. Surface pressure distribution of UP and DP for single (a), (c) and two tandem panels (b), (d) at $\alpha = 35^\circ$.

4. Concerning the primary mode of two tandem PV panels, it is observed that the vortex shedding from the UP slaps on the leading edge of the DP and is split, then merges with the wake vortex of the DP, so that the DP's fluctuating lift is larger than that of the UP's fluctuating lift. Regarding the second-order mode, for small inclined angles ($\alpha \leq 35^\circ$), the small-scale vortex intensity between the gaps increases with the increase of α, which enhances the pressure fluctuations on the up-surface of UP and the down-surface of DP. In addition, the wake flow of UP has a more pronounced tilt-upward jet trend than that of a single PV panel. For the inclined angle of 55°, the vortex from the UP bypasses the DP, while the vortex shedding from the DP is inhibited, thus reducing the fluctuating lift of DP. Accordingly, the UP protects the DP against wind vibration at large inclined angles. This study mainly studies the effect of the downstream gap spacing and inclined angle of two tandem PV panels on wind load, without considering the potential effect of the lateral spacing on wind load when PV panels are arranged side by side. Future research will further explore the effect of lateral spacing on the wind load of PV arrays, providing a more comprehensive theoretical basis for the optimal design of PV panels.

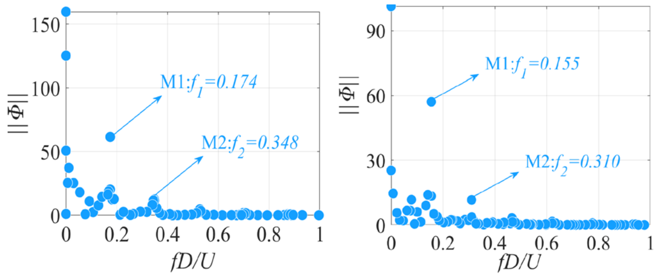

(a) Single panel (b) Two tandem panels

FIG. 16. Comparison of mode energy spectra of single (a) and tandem inclined panels (b) at $\alpha = 55^\circ$.

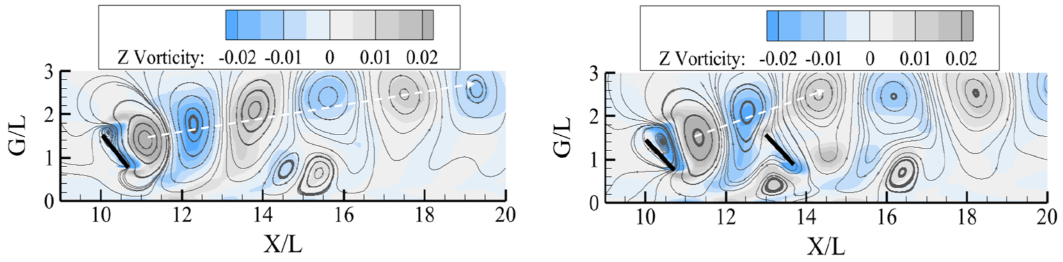

(a) M1 (b) M1

FIG. 17. Vorticity modes of the first order for the single panel (a) and two tandem inclined panels (b) at $\alpha = 55°$.

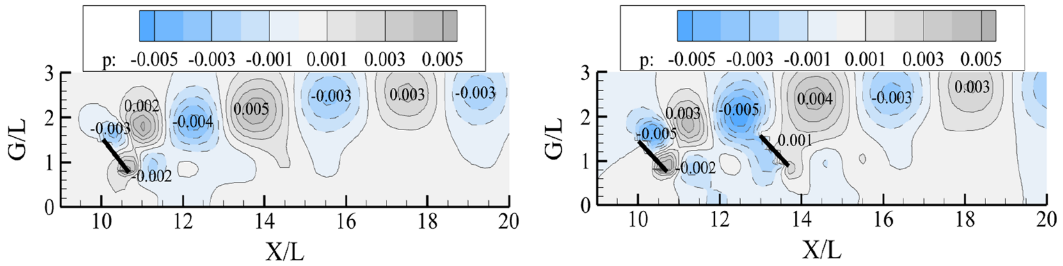

(a) M1 (b) M1

FIG. 18. Pressure modes of the first order for the single panel (a) and two tandem inclined panels (b) at $\alpha = 55°$.

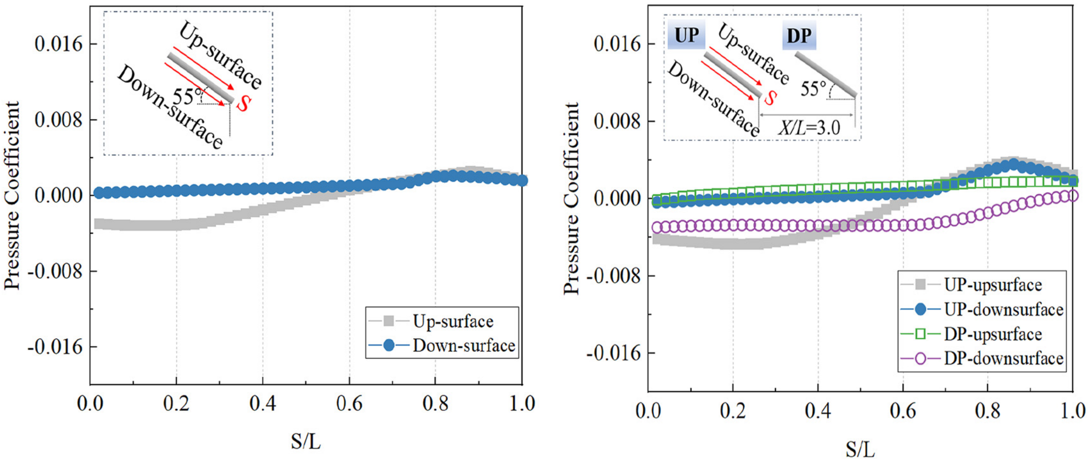

(a) M1 (b) M1

FIG. 19. Surface pressure distribution of UP and DP for single (a) and two tandem panels (b) at $\alpha = 55°$.

ACKNOWLEDGMENTS

The authors would like to thank to the support of Hainan Provincial Natural Science Foundation of China (Grant No. 524QN224) and the Natural Science Foundation of Heilongjiang Province China (Grant No. LH 2020E010). The numerical calculations in this paper have been done on Hefei advanced computing center.

AUTHOR DECLARATIONS

Conflict of Interest

The authors have no conflicts to disclose.

Author Contributions

Tingting Liu: Data curation (equal); Investigation (equal); Methodology (equal); Writing – original draft (equal); Writing –

review & editing (equal). **Hanning Mi:** Conceptualization (equal); Investigation (equal); Resources (equal); Supervision (equal); Validation (equal); Writing – review & editing (equal). **Yifeng Ai:** Data curation (equal); Formal analysis (equal); Validation (equal). **Hongfu Zhang:** Data curation (equal); Funding acquisition (equal); Project administration (equal). **Daocheng Zhou:** Formal analysis (equal); Investigation (equal); Project administration (equal); Resources (equal). **Lei Zhou:** Conceptualization (equal); Methodology (equal); Project administration (equal); Software (equal).

DATA AVAILABILITY

The data that support the findings of this study are available from the corresponding author upon reasonable request.

REFERENCES

[1] G. Bitsuamlak and A. Aly, "Aerodynamics of ground-mounted solar panels: Test model scale effects," J. Wind Eng. Ind. Aerodyn. **123**, 250–260 (2013).

[2] C. Jubayer and H. Hangan, "A numerical approach to the investigation of wind loading on an array of ground mounted solar photovoltaic (PV) panels," J. Wind Eng. Ind. Aerodyn. **153**, 60 (2016).

[3] A. M. Aly, "On the evaluation of wind loads on solar panels: The scale issue," Sol. Energy **135**, 423–434 (2016).

[4] N. Quyen and N. Duc, "Vibration and nonlinear dynamic response of nanocomposite multi-layer solar panel resting on elastic foundations," Thin-Walled Struct. **177**, 109412 (2022).

[5] A. Agarwal, H. Irtaza, and A. Zameel, "Numerical study of lift and drag coefficients on a ground-mounted photo-voltaic solar panel," Mater. Today: Proc. **4**, 9822–9827 (2017).

[6] A. Abiola, H. Hangan, and K. Siddiqui, "Experimental investigation of wind effects on a standalone photovoltaic (PV) module," Renewable Energy **78**, 657–665 (2015).

[7] H. Irtaza and A. Agarwal, "CFD simulation of turbulent wind effect on an array of ground-mounted solar PV panels," J. Inst. Eng. India Ser. A **99**, 205 (2018).

[8] A. Xu, W. Ma, H. Yuan, and L. Lu, "The effects of row spacing and ground clearance on the wind load of photovoltaic (PV) arrays," Renewable Energy **220**, 119627 (2024).

[9] C. Jubayer and H. Hangan, "Numerical simulation of wind effects on a stand-alone ground mounted photovoltaic (PV) system," J. Wind Eng. Ind. Aerodyn. **134**, 56–64 (2014).

[10] M. Shademan, R. Barron, R. Balachandar, and H. Hangan, "Numerical simulation of wind loading on ground-mounted solar panels at different flow configuration," Can. J. Civ. Eng. **41**, 728 (2014).

[11] W. Warsido, G. Bitsuamlak, J. Barata, and A. Chowdhury, "Influence of spacing parameters on the wind loading of solar array," J. Fluids Struct. **48**, 295 (2014).

[12] T. Kray and D. Markus, "Peak wind loads on single-axis PV tracking systems," in Proceedings of the 15th International Conference on Wind Engineering, Beijing, China, 2019.

[13] A. C. Sauca, T. Milchis, and F. Z. Gobesz, "Wind loading on solar panels," Műszaki Tudományos Közlemények **10**(1), 73–78 (2019).

[14] U. Winkelmann, C. Kämper, R. Höffer, P. Forman, M. Ahrens, and P. Mark, "Wind actions on large-aperture parabolic trough solar collectors: Wind tunnel tests and structural analysis," Renewable Energy **146**, 2390 (2020).

[15] W. Ma, W. Zhang, X. Zhang, W. Chen, and Q. Tan, "Experimental investigations on the wind load interference effects of single-axis solar tracker arrays," Renewable Energy **202**, 566 (2023).

[16] A. Mjalled, M. Hassan, J. Boldocký, M. Gulan, and M. Mönnigmann, "Improved neural ordinary differential equation-based reduced model for impinging jet using wall shear stress," Phys. Fluids **36**, 115140 (2024).

[17] Y. Duan, H. Liu, H. Liu, H. Chen, and C. Sun, "Numerical study of wave resonance characteristics in gaps of a floating array," Phys. Fluids **36**, 117148 (2024).

[18] T. Nonomura, K. Nankai, Y. Iwasaki, A. Komuro, and K. Asai, "Quantitative evaluation of predictability of linear reduced-order model based on particle-image-velocimetry data of separated flow field around airfoil," Exp. Fluids **62**, 112 (2021).

[19] M. Verma and A. De, "Flow dynamics of the transversely oscillating tapered circular cylinder under vortex-induced vibrations at low Reynolds number," Phys. Fluids **36**, 103603 (2024).

[20] Q. Zhu, H. Li, H. Zhu, L. Zhou, K. T. Tse, and H. Zhang, "Koopman mode analysis on discovering distributed energy transfer of post-transient flutter of a bluff body," Ocean Eng. **309**, 118557 (2024).

[21] J. Wang and J. Wang, "Wake-induced transition in the low-Reynolds-number flow over a multi-element airfoil," J. Fluid Mech. **915**, A28 (2021).

[22] L. Qiao, Y. Zhao, L. Zhou, Y. Ai, Q. Zhu, and H. Zhang, "Coherence mode and Floquet analysis on flow past a rectangular cylinder with small angle of attack," Phys. Fluids **36**(12), 123616 (2024).

[23] G. He, J. Wang, C. Pan, L.-H. Feng, Q. Gao, and A. Rinoshika, "Vortex dynamics for flow over a circular cylinder in proximity to a wall," J. Fluid Mech. **812**, 698–720 (2017).

[24] D. Dung, D. Nguyen, T. Nguyen Van, and I. Ngo, "Low-Reynolds-number wake of three tandem elliptic cylinders," Phys. Fluids **34**, 043605 (2022).

[25] Y. Bao, Q. Wu, and D. Zhou, "Numerical investigation of flow around an inline square cylinder array with different spacing ratios," Comput. Fluids **55**, 118–131 (2012).

[26] R. Nepali, P. Huan, Z. Han, D. Zhou, H. Yang, J. Tu, Y. Zhao, and Y. Bao, "Two-degree-of-freedom vortex-induced vibrations of two square cylinders in tandem arrangement at low Reynolds numbers," J. Fluids Struct. **97**, 102991 (2020).

[27] P. Sellappan and T. Pottebaum, "Wake modes of rotationally oscillating cylinders at Re = 150," J. Fluids Struct. **46**, 29–41 (2014).

[28] S. A. Orszag, "Analytical theories of turbulence," J. Fluid Mech. **41**, 363–386 (1970).

[29] C. Cantwell, D. Moxey, A. Comerford, A. Bolis, G. Rocco, G. Mengaldo, D. De Grazia, S. Yakovlev, J.-E. Lombard, D. Ekelschot, B. Jordi, H. Xu, Y. Mohamied, C. Eskilsson, B. Nelson, P. Vos, C. Biotto, R. Kirby, and S. Sherwin, "Nektar++: An open-source spectral/*hp* element framework," Comput. Phys. Commun. **192**, 205 (2015).

[30] D. Moxey, C. Cantwell, Y. Bao, A. Cassinelli, G. Castiglioni, S. Chun, E. Juda, E. Kazemi, K. Lackhove, J. Marcon, G. Mengaldo, D. Serson, M. Turner, H. Xu, J. Peiro, R. Kirby, and S. Sherwin, "Nektar++: Enhancing the capability and application of high-fidelity spectral/*hp* element methods," Comput. Phys. Commun. **249**, 107110 (2020).

[31] V. Saini, H. Xia, and G. Page, "Comparison of finite-volume and spectral/*hp* methods for large-eddy simulation of combustor port flow," AIAA J. **60**, 4367 (2022).

[32] D. Yang, B. Pettersen, H. Andersson, and V. Narasimhamurthy, "Vortex shedding in flow past an inclined flat plate at high incidence," Phys. Fluids **24**, 084103 (2012).

[33] Y. Tominaga, A. Mochida, R. Yoshie, H. Kataoka, T. Nozu, M. Yoshikawa, and T. Shirasawa, "AIJ guidelines for practical applications of CFD to pedestrian wind environment around buildings," J. Wind Eng. Ind. Aerodyn. **96**, 1749–1761 (2008).

[34] S. Foshat, "Numerical investigation of the effects of plasma actuator on separated laminar flows past an incident plate under ground effect," Aerosp. Sci. Technol. **98**, 105646 (2020).

[35] A. Yifeng, L. Zhou, K. Tse, and H. Zhang, "Interference and ground effects on flow past two inclined flat plates in tandem arrangement," Ocean Eng. **270**, 113653 (2023).

[36] L. Formaggia and F. Nobile, "Stability analysis of second-order time accurate schemes for ALE–FEM," Comput. Methods Appl. Mech. Eng. **193**, 4097–4116 (2004).

[37] A. Naseri, I. González, A. Amani, C.-D. Perez Segarra, and A. Oliva, "A second-order time accurate semi-implicit method for fluid–structure interaction problems," J. Fluids Struct. **86**, 135 (2019).

[38] C. Geuzaine and J.-F. Remacle, "GMSH: A 3-D finite element mesh generator with built-in pre- and post-processing facilities," Int. J. Numer. Methods Eng. **79**, 1309–1331 (2009).

[39] A. Wynn, D. Pearson, B. Ganapathisubramani, and P. Goulart, "Optimal mode decomposition for unsteady flows," J. Fluid Mech. **733**, 473 (2013).

[40] Z. Li, C. Lan, L. Jia, and Y. Ma, "Ground effects on separated laminar flows past an inclined flat plate," Theor. Comput. Fluid Dyn. **31**, 127 (2017).

[41] F. Najjar and S. Balachandar, "Low-frequency unsteadiness in the wake of a normal flat plate," J. Fluid Mech. **370**, 101–147 (1998).

[42] F. Najjar and S. Vanka, "Effects of intrinsic three-dimensionality on the drag characteristics of a normal flat plate," Phys. Fluids **7**, 2516–2518 (1995).

[43] H. Zhang, L. Zhou, T. Liu, Z. Guo, and F. Golnary, "Dynamic mode decomposition analysis of the two-dimensional flow past two transversely in-phase oscillating cylinders in a tandem arrangement," Phys. Fluids **34**, 033602 (2022).